17A.5 OPTIMIZING LIDAR SCANNING STRATEGIES FOR WIND ENERGY TURBULENCE MEASUREMENTS

Jennifer F. Newman[1]*, Timothy A. Bonin[1], Petra Klein[1], Sonia Wharton[2], and Philip B. Chilson[1]
[1]School of Meteorology, University of Oklahoma, Norman, OK
[2]Atmospheric, Earth and Energy Division, Lawrence Livermore National Laboratory, Livermore, CA

1. INTRODUCTION

Initially, it was assumed that the power produced by a wind turbine depends only on the average wind speed at the turbine hub height. However, recent studies have indicated that turbine power production depends on a variety of other factors, including the thermodynamic stability of the atmosphere (e.g., Sumner and Masson 2006; Wharton and Lundquist 2012), turbulence (e.g., Elliott and Cadogan 1990), and the entire wind speed profile intercepted by the turbine blades, i.e., across the rotor-disk swept area (e.g., Wagner et al. 2009). Wharton and Lundquist (2012) showed that the average power produced by a wind turbine at a West Coast wind farm differed by as much as 20% according to the stability and turbulence present in the atmosphere (Fig. 1). This difference in power production is extremely important for utility operators, who must decide which combination of energy sources will best meet consumer demand at a given time. In some areas, penalties are issued to wind farm owners if the amount of available wind energy is overestimated and the wind power supply does not meet the energy demand (Lundquist et al. 2010).

An accurate wind resource assessment requires an estimate of wind speeds across the heights spanned by a turbine rotor disk (typically 40 to 120 m above ground level; AGL). Traditionally, these measurements have been made with cup anemometers on tall meteorological towers. However, as turbine hub heights extend further into the atmosphere, it has become more difficult and costly to build tall towers that reach these heights. In response to this issue, remote sensing devices have recently emerged as an alternative to tall towers and are now commonly employed in wind energy studies.

* *Corresponding author address:* Jennifer F. Newman, School of Meteorology, University of Oklahoma, 120 David L. Boren Blvd., Norman, OK 73072. E-mail: jennifer.newman@ou.edu

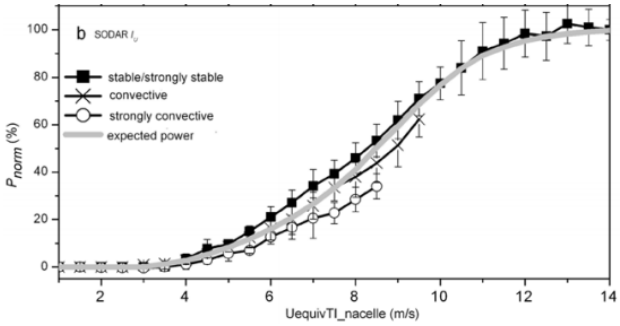

Figure 1: Normalized power produced by a wind turbine as a function of equivalent, or rotor disk-averaged, wind speed, and atmospheric stability regime. Stable regimes were associated with low amounts of turbulence, while convective and strongly convective regimes were associated with high amounts of turbulence. From Wharton and Lundquist (2012).

One frequently used remote sensing instrument is a Doppler lidar (light detection and ranging), which utilizes the Doppler shift of backscattered laser energy to estimate the wind speed within a volume of air. Lidars can measure wind speeds up to several hundred meters above the ground and are ideally suited for estimating wind speeds across a typical turbine rotor disk area. However, the measurement of turbulence with remote sensing devices such as lidars is not as straightforward. Lidars estimate the mean wind speed of volumes of air that are typically 10–30 meters in length, and thus cannot measure small-scale, high-frequency turbulent motions. In addition, most lidar scanning strategies were designed to measure mean wind speeds, not turbulence. Atmospheric turbulence is extremely important in the wind energy field; turbulence has profound effects on turbine power production and can induce damaging loads on turbine blades (e.g., Kelley et al. 2006). Thus, in order to be viewed as a viable alternative to meteorological towers, remote sens-

ing devices most be able to accurately measure turbulence.

This work explores the use of various lidar scanning strategies to measure turbulence in the lower boundary layer, i.e., the portion of the atmosphere that is most important for wind energy studies. To this end, a feasibility study was carried out during the summer of 2013 to evaluate different lidar scanning strategies. Two scanning lidars were deployed at the Southern Great Plains Atmospheric Radiation Measurement (ARM) site, a field measurement site located in northern Oklahoma and instrumented with various in-situ and remote sensing devices. These lidars were used in conjunction with a vertically-scanning, commercially available WindCube lidar and an additional scanning lidar located permanently at the ARM site to test different scanning strategies.

While the scanning strategy of the WindCube lidar could not be changed, the scanning strategies of the three scanning lidars were entirely user-defined, allowing for the optimization of scanning strategies for turbulence measurements. Three different scanning strategies were tested during the experiment: a tri-Doppler technique, a novel six-beam technique, and a "virtual tower" technique, where all three scanning lidars were used to measure wind speed and turbulence at several different heights above the WindCube lidar. The turbulence and mean wind speeds measured with these scanning strategies were compared to identical parameters measured by the WindCube lidar and sonic anemometers on a 60-m meteorological tower at the ARM site. In this paper, only results from the tri-Doppler and six-beam scanning strategies are discussed.

2. BACKGROUND

2.1. *Experimental Overview*

The field experiment took place from 12 June to 3 July 2013 at the Southern Great Plains ARM site near Lamont, Oklahoma (Fig. 2). The site is situated in flat, fairly uniform terrain in an area of Oklahoma with high wind resource potential; in fact, a large operational wind farm is located in the same region. Strong wind speeds in the region are often associated with the nocturnal low-level jet (LLJ), a common phenomenon in the Southern Great Plains region that experiences a climatological maximum during the summer months in Oklahoma (Bonner 1968; Song et al. 2005).

Locations of the various instruments used in the study are shown in Fig. 3. The OU Halo lidar and the ARM Halo lidar are the scanning lidars owned by the University of Oklahoma (OU) and the ARM site, respectively. The Galion lidar is a lidar rented by OU that has identical hardware to the two scanning Halo lidars.

2.2. *Instrumentation*

The three scanning lidars (OU Halo, ARM Halo, and Galion) are pulsed heterodyne lidars equipped with a scanner that can move in both azimuth and elevation. The moveable scanner allows for the implementation of user-defined scanning strategies. In contrast, the WindCube lidar uses a rotating prism to steer the lidar beam in azimuth and is limited to scanning at a fixed elevation angle. Technical specifications of the lidars are summarized in Table 1. Detailed information for the Halo system can be found in Pearson et al. (2009).

Data from a 60-m meteorological tower were also available during the experiment. Gill Windmaster Pro 3-D sonic anemometers and Licor infrared gas analyzers are mounted on the tower at 25 and 60 m. A 4-m flux tower is also located near the base of the 60-m tower and collects surface meteorological data in addition to sonic anemometer data. More information can be found in the instrument handbook: `http://www.arm.gov/publications/tech_reports/handbooks/co2flx_handbook.pdf`. Sonic anemometer data were collected at a frequency of 10 Hz.

Unfortunately, sonic anemometer data were only available up to 60 m AGL at the ARM site, while the first useable range gate of the scanning lidars was centered at 105 m AGL. Although lidar data from some of the scanning strategies were available at lower heights, the majority of wind speed data from the scanning lidars did not coincide with any sonic anemometer data. This made it difficult to verify the accuracy of the wind speeds and variance values measured by the scanning lidars. Thus, the summer multi-lidar experiment was treated as a feasibility study rather than a definitive experiment on lidar turbulence scanning strategies. Best practices learned from the summer lidar experiment were later applied to the design and execution of a similar experiment at the Boulder Atmospheric Observatory, a site in Colorado with a heavily instrumented 300-m tower.

Figure 2: Google Earth image of the state of Oklahoma. Location of Southern Great Plains ARM site is denoted by red marker.

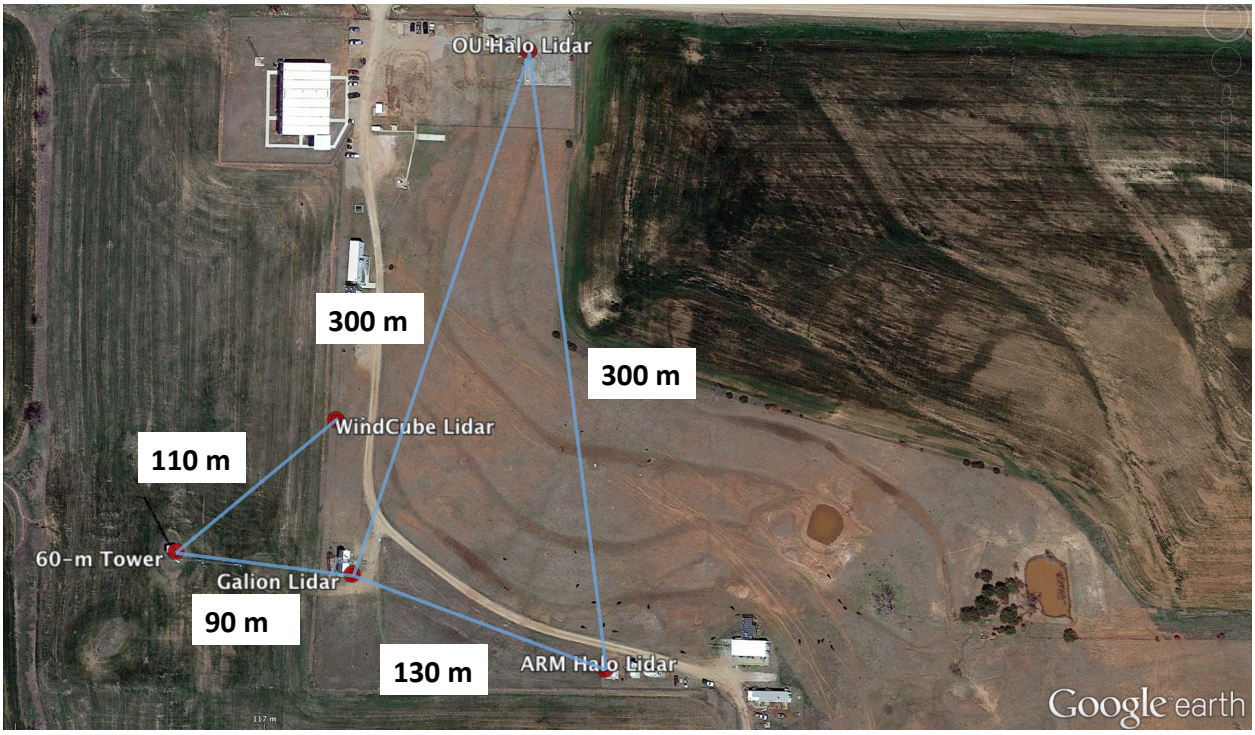

Figure 3: Google Earth image of the central facility of the Southern Great Plains ARM site. Instrument locations are denoted by red markers. Approximate distances between instruments are indicated by blue lines and labels.

2.3. *Lidar Scanning Strategies*

i. WindCube Scanning Strategy The WindCube lidar used in the experiment measures wind speed with a Doppler Beam-Swinging (DBS) technique (e.g., Strauch et al. 1984). In each DBS scan, the lidar beam is pointed in the four cardinal directions (north, south, east, and west), then

Lidar Specifications		
	Leosphere WindCube v2	**Halophotonics Streamline Pro**
Wavelength	1.5 μm	1.5 μm
Min. Range	40 m	105 m
Max. Range	200 m	9.6 km (4 km for Galion)
Range Resolution	20 m	Variable - Typically 18–30 m
Sampling Rate	1 Hz	1 Hz
Scanning Azimuth Angles	0, 90, 180, 270°	User-defined: 0–360°
Scanning Elevation Angles	62, 90°	User-defined: 0–90°

Table 1: Technical specifications for lidars used in scanning strategy experiment. Unless otherwise noted, specifications for Galion lidar are identical to those listed for Halo lidar. Azimuth angles are measured from true north and elevation angles are measured from ground level.

pointed vertically. Based on geometrical relations, the u, v, and w wind components can be derived from the radial velocities measured at the different beam locations.

At each beam location, 20,000 pulses of laser energy are emitted into the atmosphere. The signal that is returned to the WindCube is separated into range gates and several Doppler spectra are produced for each range gate. The Doppler spectra from each range gate are then averaged to produce a smooth spectrum. The peak frequency in the averaged spectrum is finally related to the radial velocity at each beam location and range gate. This process takes just under one second per beam location, such that a full DBS scan is completed approximately every four seconds. However, the WindCube velocity algorithm calculates the u, v, and w components every one second using the current radial velocity and the radial velocities obtained from the previous four beam locations (Cariou and Boquet 2010).

Three major problems arise when using this technique to measure turbulence (e.g., Sathe et al. 2011; Sathe and Mann 2012a). The first is the volume averaging inherent in remote sensing technology for any kind of scanning strategy; as previously discussed, the velocity measured by a lidar is the weighted average of all aerosol velocities within the probe volume. Thus, turbulence scales that are smaller than the probe volume cannot be measured accurately. Next, this type of scanning technique assumes that the velocity is uniform throughout the scanning circle formed by the various beam positions. For low heights and uniform terrain, this assumption is likely valid at times, but becomes invalid for higher measurement heights and complex terrain. (The WindCube v2 scans with an elevation angle of 62°, which translates to a scanning circle diameter of approximately 106 m at a measurement height of 100 m.) Finally, the use of only four horizontal beams to calculate three-dimensional turbulence introduces systematic errors. Sathe and Mann (2012a) show that the calculated variance values of the wind components u, v, and w are contaminated by the cross-components of the Reynolds stress tensor; i.e., the variance of the v component has contributions from not just the v component of the wind, but the u and w components as well.

While volume averaging decreases the value of the lidar-estimated variance, the Reynolds stress tensor contamination increases the variance (Sathe et al. 2011). Thus, the variance contamination can often mask the effects of volume averaging, causing the lidar-estimated variance to be higher than the variance that is actually being measured by the lidar. In unstable environments, where turbulent motions tend to occur on larger spatial scales (e.g., Stull 2000), the effects of variance contamination can overcome the effects of volume averaging and cause the lidar to overestimate the true value of the variance (Sathe et al. 2011).

Examples of variance estimated from the WindCube lidar and the 60-m sonic anemometer are shown in Fig. 4. The variance components $\overline{u'^2}$, $\overline{v'^2}$, and $\overline{w'^2}$ were defined as follows:

$$\overline{u_i'^2} = \overline{(u_i - \overline{u_i})^2} \tag{1}$$

where the different variance components are given for i = 1, 2, 3 and the overbar denotes a

temporal average. For the time series plots in Fig. 4, a 30-min. temporal average was used. The turbulence kinetic energy (TKE) is defined by the following equation (Stull 2000):

$$TKE = \frac{1}{2}(\overline{u'^2} + \overline{v'^2} + \overline{w'^2}) \quad (2)$$

The lidar-estimated u and v variance closely follow the variance estimated by the sonic anemometer for the first portion of the time series, until approximately 14 UTC (11 am local time). After this point, the lidar appears to overestimate the u and v variance in comparison to the sonic anemometer. In contrast, the lidar underestimates the w variance throughout the entire time series. It is likely that as the atmosphere became unstable in the late afternoon, the effects of volume averaging on the lidar-estimated variance were overcome by the effects of the variance contamination, causing the lidar to measure higher variance than the sonic anemometer. The w variance component does not seem to be as affected by variance contamination, likely because turbulence scales in the vertical direction are typically much smaller than turbulence scales in the horizontal direction and volume averaging is more prominent (Sathe et al. 2011). These variance trends are characteristic of most days from the experiment and are in agreement with the theoretical findings of Sathe and Mann (2012b). It is interesting to note that the lidar-derived TKE values are quite close to the sonic TKE values throughout the time series, despite the differences in overestimates and underestimates in the different variance components. Thus, it is important to employ caution when using TKE as a proxy for turbulence, as the three variance components are affected differently by different factors.

ii. Tri-Doppler Technique The three scanning strategies tested in the experiment were designed to mitigate the turbulence errors induced by a standard DBS scan. In the first strategy, the tri-Doppler technique, the beams of the three scanning lidars were steered toward approximately the same point in space to avoid the use of a scanning circle. Although the effects of averaging within the probe volume cannot be mitigated in this way, the tri-Doppler technique allows for the measurement of turbulence within a small area of space rather than a large scanning circle and does not require the assumption of horizontal homogeneity within a scanning circle.

Since three lidars are used in the tri-Doppler technique and there are three unknown wind components, u, v, and w, a set of three equations can be used to solve for the wind components. For this experiment, the dual-Doppler lidar technique described by Calhoun et al. (2006) was extended to include an additional lidar. In this technique, the radial velocity measured by each lidar is written as the dot product between the true three-dimensional velocity vector and the unit vector of the lidar system:

$$\begin{aligned} v_{r,lidar} &= \mathbf{r_{lidar}} \cdot \mathbf{U} \\ &= ucos(\phi)sin(\theta) + vcos(\phi)cos(\theta) \\ &+ wsin(\phi) \end{aligned} \quad (3)$$

where u, v, and w are the zonal, meridional, and vertical components of the velocity, respectively, ϕ is the elevation angle of the lidar beam, and θ is the azimuthal angle of the lidar beam, measured from true north. After the radial velocity equations are written for each scanning lidar, a set of three equations and three unknowns is obtained and the equations can be solved to estimate the three true wind components.

iii. Six-Beam Technique Sathe (2012) developed a new lidar scanning strategy that minimizes the variance contamination caused by the DBS technique. A brief description of the development of the technique is presented here.

Following Eberhard et al. (1989), the variance of the radial velocity measured by a Doppler lidar can be written as follows:

$$\begin{aligned} \overline{v_r'^2} = \overline{u'^2}sin^2\phi cos^2\theta &+ \overline{v'^2}sin^2\phi sin^2\theta + \overline{w'^2}cos^2\phi \\ + 2\overline{u'v'}sin^2\phi sin\theta cos\theta &+ 2\overline{u'w'}sin\phi cos\phi cos\theta + \\ 2\overline{v'w'}sin\phi cos\phi sin\theta & \end{aligned} \quad (4)$$

where $\overline{u'v'}$, $\overline{u'w'}$, and $\overline{v'w'}$ are the covariances of the velocity components, and θ and ϕ refer to the azimuth and elevation angle of the lidar beam, as before. For each beam position (i.e., for each combination of θ and ϕ), the variances and covariances create a set of six unknown quantities. In order to independently solve for the six unknown variables, Sathe (2012) creates a set of six equations with six different combinations of θ and ϕ. The optimum values for θ and ϕ are selected by using a minimization algorithm to determine the

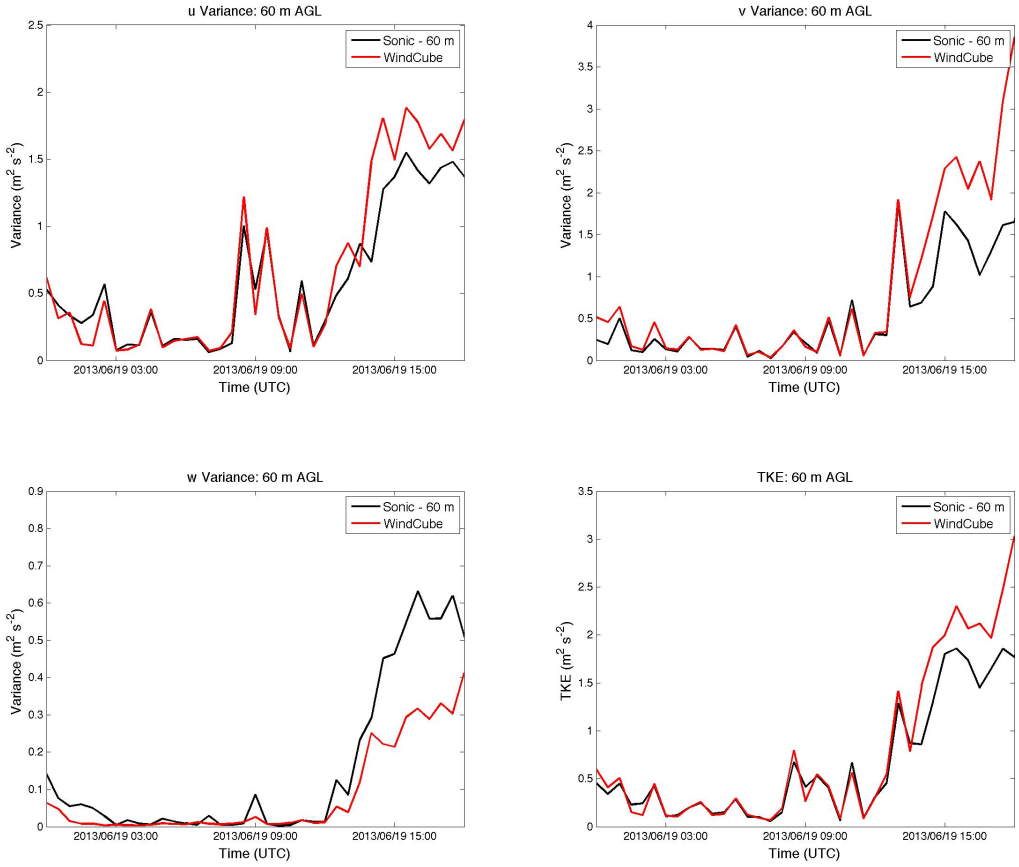

Figure 4: Time series plots of variance components and TKE measured by the WindCube lidar and 60-m sonic anemometer at the ARM site.

combination of parameters that minimizes the random errors in the variance estimates. The optimal configuration is as follows: five beams at an elevation angle of 45° that are equally spaced 72° apart (i.e., located at azimuths of 0, 72, 144, 216, and 288°), and one vertically pointed beam. This scanning strategy is hereafter referred to as the six-beam technique.

iv. Virtual Tower Technique The final scanning strategy tested in the experiment involved the use of all three scanning lidars to build a "virtual tower" over the WindCube lidar. This strategy was identical to the tri-Doppler technique, except the beams were moved to different heights AGL every 10 min. Thus, a virtual tower was formed with mean wind speed and turbulence measurements at several different heights, similar to a meteorological tower.

3. Scanning Strategy Evaluation

3.1. *Quality Control and Data Processing*

i. Spike Filter Before being used for mean wind speed or variance calculations, the raw 10 Hz sonic anemometer data were passed through a spike filter to eliminate noisy data. Data points that were more than six standard deviations away from the 100-second running mean were set to the value of the running mean.

For the lidar data, the spike filter developed by Højstrup (1993) and adapted by Vickers and Mahrt (1997) was used. A 10-min. moving window was shifted through the raw lidar data one point at a time. For each window, the mean was calculated and any point that was more than 3.5 standard deviations from the mean was flagged as a possible spike and removed from the dataset. This process was repeated until no more spikes were detected.

For each iteration, the factor of 3.5 standard deviations was increased by 0.1 standard deviations.

ii. Signal-to-Noise Ratio and Precipitation Filters By default, WindCube radial velocities that were associated with Signal-to-Noise ratios (SNRs) lower than -23 dB were flagged as missing values. An SNR filter was not used with the scanning lidar systems, as most SNR values are above -20 dB in the lowest few hundred meters AGL for the Halo lidar system (Pearson et al. 2009).

Doppler lidars use the backscattered radiation from atmospheric aerosols to determine the radial wind speed and are adversely affected by the presence of precipitation particles, which can result in beam attenuation and increased vertical velocities (e.g., Huffaker and Hardesty 1996; Pearson et al. 2009). Thus, lidar data were not used when the rain gauge at the ARM site recorded precipitation.

iii. Time and Location Synchronization Multi-lidar scanning strategies require that the scanning lidars are synchronized in time and that the exact locations of the lidars are known (Calhoun et al. 2006). The lidars must be scanning the same volume of air at the same time in order to accurately combine the lidar data in velocity variance calculations.

The instruments at the ARM site are located on the same network and are thus synchronized in time with each other. Timestamps are derived from the computer clocks associated with the various instruments, and the computer clocks are updated regularly to avoid time drifting errors. The two additional scanning lidars (the OU Halo lidar and the Galion lidar) are also synched with internal computer clocks. At the beginning of the experiment, it was discovered that the Galion computer clock was consistently slower than the OU Halo computer clock by approximately 48 seconds and the ARM computer clock associated with the ARM Halo lidar was 52 seconds faster than the OU clock. These timestamps were corrected in post-processing. The WindCube lidar constantly derives its timestamps from satellite information, so it was assumed that the WindCube timestamps were consistent and accurate.

Lidar alignment was verified following the technique of Calhoun et al. (2006). At the start of the experiment, the OU Halo lidar and the Galion lidar beams were pointed toward the 60-m tower for several minutes. Short range-height indicator (RHI) scans were completed at low elevation angles, with samples taken every 0.5°. These RHI scans were repeated until the tower appeared as a hard target on the lidar display. The azimuthal angle at which the tower appeared was recorded and compared to the expected azimuthal angle calculated from Google Earth. The difference between these two angles was then used to adjust the bearing of the lidars such that true north corresponded to the 0° azimuthal angle.

iv. Coordinate Rotation Before derived products, such as variance, were calculated, a coordinate rotation was applied to the lidar data. Following the procedure outlined by Wilczak et al. (2001), the data were first rotated such that the mean meridional wind speed, $\overline{v}$, was set to zero. Next, the coordinate axes were rotated such that u was aligned with the mean wind direction and $\overline{w}$ was equal to zero.

3.2. *Variance Estimation*

Several errors can arise when atmospheric variance is estimated from an in-situ or remote sensing instrument. Vickers and Mahrt (1997) discuss three types of sampling errors that can occur in the measurement of fluxes: systematic errors, random errors, and mesoscale flow variability. Vickers and Mahrt (1997) suggest several tests that can be performed to determine the optimal averaging times for turbulence calculations and to flag data that may affect the variance calculations. These tests were performed on data from the tri-Doppler portion of the experiment, as this was the first week of the experiment and all three scanning lidars were consistently measuring the wind speed at the same height AGL.

Systematic errors occur when the largest turbulent transport scales are not measured and the variance is typically underestimated as a result. In order to avoid systematic errors, Vickers and Mahrt (1997) recommend determining the optimal local averaging scale, L, which represents the largest scale of turbulent motions that are included in variance and flux calculations. For different values of L (i.e., 5 min., 10 min., etc.), the instantaneous flux $w'\phi'$ is computed, where ϕ is some atmospheric quantity, equal to $\overline{\phi} + \phi'$ and the mean quantity $\overline{\phi}$ is calculated over an averaging time L. For this work, the vector-averaged wind stress was used to determine L, as in Mahrt et al. (1996). The vector-averaged wind stress, $\langle w'\mathbf{v}'\rangle$, is defined by

the following equation:

$$\langle w'\mathbf{v}'\rangle = \left(\langle w'u'\rangle^2 + \langle w'v'\rangle^2\right)^{1/2} \quad (5)$$

where the brackets indicate an average over the length of the data record. In this work, one-hour long data records were used, as in Vickers and Mahrt (1997). Averaging times of 1, 5, 10, 15, 20, 30, and 60 min. were used for L.

The instantaneous momentum fluxes were calculated for the different values of L for each one-hour data record, then averaged over the one-hour data record to form the vector-averaged wind flux. Finally, the one-hour averaged wind stresses from each value of L were averaged over all stationary one-hour data records during the tri-Doppler portion of the experiment. Stationarity in the along-wind direction was determined by using the following metric from Vickers and Mahrt (1997):

$$RNu \equiv \frac{\delta u}{\langle u\rangle} \quad (6)$$

where u is aligned with the one-hour mean wind direction, δu is the difference in u between the start and end of the one-hour record, and $\langle u\rangle$ is the one-hour mean wind speed. The record is deemed non-stationary if the absolute value of RNu exceeds 0.50. Of the 81 records used to calculate the vector-averaged wind stress, only six records were flagged as non-stationary (approximately 7%). Most of these records were associated with frontal passages.

For the tri-Doppler data, the mean value of the vector-averaged wind stress calculated at 105 m AGL using a local averaging time of 10 min. is approximately 90% of the value of the wind stress calculated with an averaging time of one hour (the length of the data record). Thus, an averaging time of 10 min. should be sufficient to capture the variance associated with the majority of the turbulent transport eddies present in a one-hour time frame.

Random sampling errors occur as a result of the random variability of the location and strength of turbulent eddies. Following Vickers and Mahrt (1997), flux variability due to random errors and mesoscale motions can be estimated by dividing the 10-min. flux into a linear trend over the one-hour data record and the deviation from the linear trend:

$$F_i = \langle F_i\rangle + F_{tr} + F_i^* \quad (7)$$

where F_i is the 10-min. vector-averaged wind stress, $\langle F_i\rangle$ is the average 10-min. stress over the 1-hour data record, F_{tr} is the linear trend of the 10-min. stress over the 1-hour data record (minus the 1-hour mean), and F_i^* is the deviation of the 10-min. stress from the linear trend. The relative flux error, RFE, and the error due to mesoscale motions, RN, are defined as follows:

$$RFE \equiv \frac{\sigma_{F*}}{|\langle F_i\rangle|\, N^{1/2}} \quad (8)$$

and

$$RN \equiv \frac{\sigma_{F_{tr}}}{|\langle F_i\rangle|\, N^{1/2}} \quad (9)$$

where σ_{F*} is the standard deviation of the flux deviation over the 1-hour data record, $\sigma_{F_{tr}}$ is the standard deviation of the linear trend line, and N is the number of 10-min. stress values in the data record ($N = 6$ in this case). Data records where either RFE or RN exceeded 0.3 were flagged.

In order to mitigate the effects of random errors on variance calculations, Vickers and Mahrt (1997) recommend averaging turbulent fluxes over a period of time that is longer than the local averaging length, L. Thus, for records without a flag, the variance was defined as the mean value of $u_i'^2$ (calculated using L = 10 min.) over a 30-minute period. For data records with a flag, the averaging period was increased from 30 to 60 min. to reduce the effects of random errors and mesoscale variability on the wind speed variance.

3.3. *Tri-Doppler Technique*

The tri-Doppler technique was evaluated from 12 to 19 June 2013. Between approximately 0000 and 1500 UTC (7 pm and 10 am local time) every day, the OU Halo and Galion lidars were set to perform a constant horizontal stare scan at a point approximately 105 m above the ARM Halo lidar. (This height corresponds to the first useable range gate from the Halo system.) During this time, the ARM Halo lidar performed a constant vertical stare scan directly above the lidar. (For the remainder of the day, the OU Halo and Galion lidars were set to a vertical stare mode for a different experiment.) The range gate length for the OU Halo and Galion lidars was set to 30 m to match the range gates of the ARM Halo lidar. Unfortunately, the lidar alignment was not verified until the second week of the experiment, so there

was some uncertainty regarding the true bearing of the scanning lidars to the ARM Halo lidar.

After the data were collected, timestamps from the Galion and ARM Halo lidars were adjusted to match those from the OU Halo lidar. Radial velocity data from the different lidars were then interpolated to a one-second grid using a linear interpolation. Finally, the tri-Doppler technique, discussed in the previous section, was used to calculate u, v, and w every one second. Corresponding WindCube data were interpolated to the same one-second grid.

Sample time series plots of rotated raw wind speed data are shown in Fig. 5. (Note that the v and w components oscillate around 0 m s^{-1} because the coordinate rotation forces the mean v and w values to 0.) In general, the raw WindCube and tri-Doppler data correspond well to one another, both displaying large wind speed shifts at approximately 0600 and 0900 UTC in association with a cold frontal passage. The tri-Doppler data do appear to capture slightly higher-frequency fluctuations than the WindCube data, as discussed later in this section.

A time series of velocity variance and TKE from 13 June 2013 is shown in Fig. 6. While the variance measured by the two techniques is generally in agreement, some deviations do occur – at certain times, the tri-Doppler variance is larger while at other times, the WindCube variance is larger. In order to provide insight into this discrepancy, scatter plots were developed for all variance values measured during the tri-Doppler portion of the campaign. In addition, the variance was stratified by stability class according to Monin-Obukhov length, L, where $L = -\frac{u_*^3 \overline{\theta_v}}{\kappa g \overline{w'\theta_v'}}$. u_* is the friction velocity, $\overline{\theta_v}$ is the mean virtual potential temperature at the measurement height, κ is the von Kármán constant (commonly set to 0.4), g is the acceleration due to gravity, and $\overline{w'\theta_v'}$ is the heat flux measured at the surface (e.g., Arya 2001). Stability thresholds were defined as follows:

Unstable: $-600 < L < 0$
Neutral: $|L| \geq 600$
Stable: $0 \leq L < 600$

Unfortunately, maintenance work was being performed on the 60-m tower during the first week of the experiment, so the only sonic data that were consistently available throughout the evaluation of the tri-Doppler technique were from the 4-m eddy covariance tower. Thus, Obukhov length from the 4-m sonic anemometer was used to classify stability at the 105-m tri-Doppler measurement height. For all other scanning techniques, the Obukhov length at 60 m was used to classify stability.

Scatter plots of tri-Doppler variance versus WindCube variance are shown in Fig. 7. For the u variance component, the variance associated with stable conditions was quite similar for both the tri-Doppler technique and the WindCube lidar, with most points lying close to the one-to-one line. However, there was a slight tendency for the tri-Doppler technique to measure higher cross-wind variances (Fig. 7b) and lower vertical variances (Fig. 7c) in comparison to the WindCube under stable conditions. It is possible that the tri-Doppler technique was able to measure smaller scales of turbulence because it was not using a large scanning cone like the WindCube lidar. The lack of averaging over a scanning circle would generally lead to the measurement of higher v and w variance values, as the cross-wind and vertical turbulent eddies tend to occur on much smaller scales than the alongwind turbulent eddies, particularly under stable conditions (e.g., Panofsky 1962). It is unclear why the WindCube lidar measured slightly higher values of the w variance under stable conditions. The WindCube did have a smaller range gate length (20 m) in comparison to the scanning lidars (30 m), so the difference in w variance may have been largely affected by volume averaging.

The variance associated with unstable conditions did not appear to follow any kind of consistent trend, possibly because there were fewer data points under unstable conditions. (The majority of the variances were associated with stable conditions due to the lack of access to the scanning lidars during the daytime, convective period.) However, the WindCube tended to measure higher v variances under convective conditions. It is possible that this variance overestimation is due to variance contamination, which is most prevalent during unstable periods (Sathe et al. 2011).

Although the WindCube lidar and the ARM Halo lidar (where the tri-Doppler scans were directed) were separated by approximately 150 m (Fig. 3), winds were primarily southeasterly throughout the duration of the tri-Doppler experiment, which is along the orientation of the lidars. Thus, if Taylor's frozen turbulence hypothesis (Taylor 1938) is valid, the lidars should sample the same turbulent eddies as they move along with the mean wind (Panofsky and Dutton 1984). Indeed, the along-wind variance was quite similar for both techniques, even though the measurements

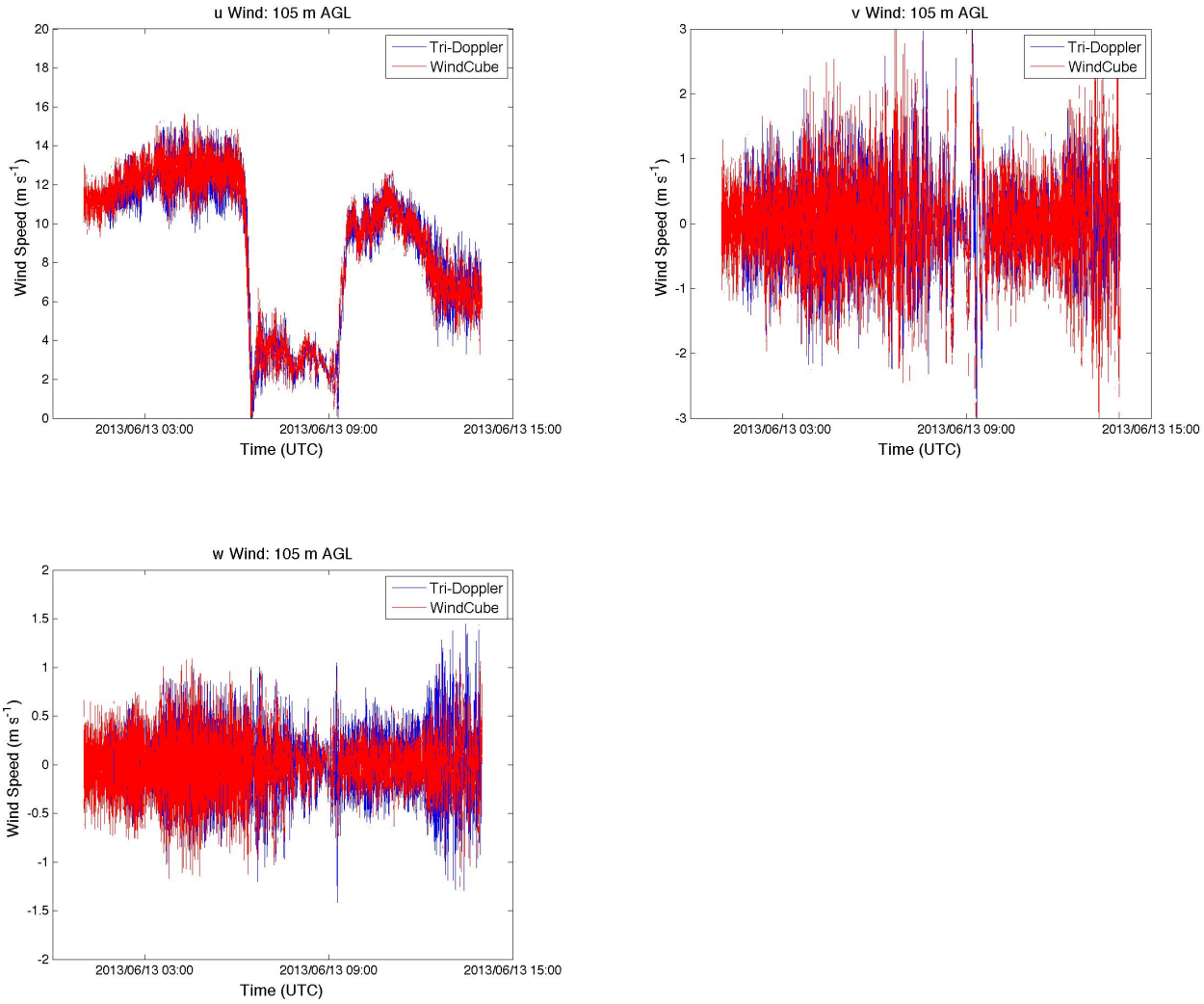

Figure 5: Time series of raw rotated wind speed from WindCube lidar and tri-Doppler technique at 105 m AGL on 13 June 2013.

were taken at different locations (Fig. 7a). More substantial differences occurred for the cross-wind and vertical variance components (Figs. 7b–7c).

Average velocity spectra were also calculated for the two different scanning techniques. First, the raw velocity data were separated into 30-min. blocks. Missing values were filled in using linear regression. The 30-min. mean was removed and a Fourier transform was performed on the velocity deviations. Finally, all 30-min. spectra for each stability class were averaged to produce average spectra. Averaged spectra for unstable and stable conditions are shown in Figs. 8 and 9.

The large dip in the u and v WindCube spectra that occurs at approximately 0.25 Hz corresponds to the time it takes the WindCube lidar to complete a full scan (approximately 4 seconds). Every four seconds, the WindCube observations of u and v become completely independent again, so the variance for the four-second time period is greatly reduced. Because the w calculation changes with the addition of each new beam, the dip is not as evident in the w spectra.

The unstable spectra agree well at the lower frequencies, but the WindCube u and v spectra have slightly higher energy for the high frequencies (Fig. 8). Cañadillas et al. (2011) found similar results when comparing averaged WindCube spectra to sonic anemometer spectra and attribute the increase in spectral energy to variance contamination. Indeed, Cañadillas et al. (2011) showed that this energy increase was not

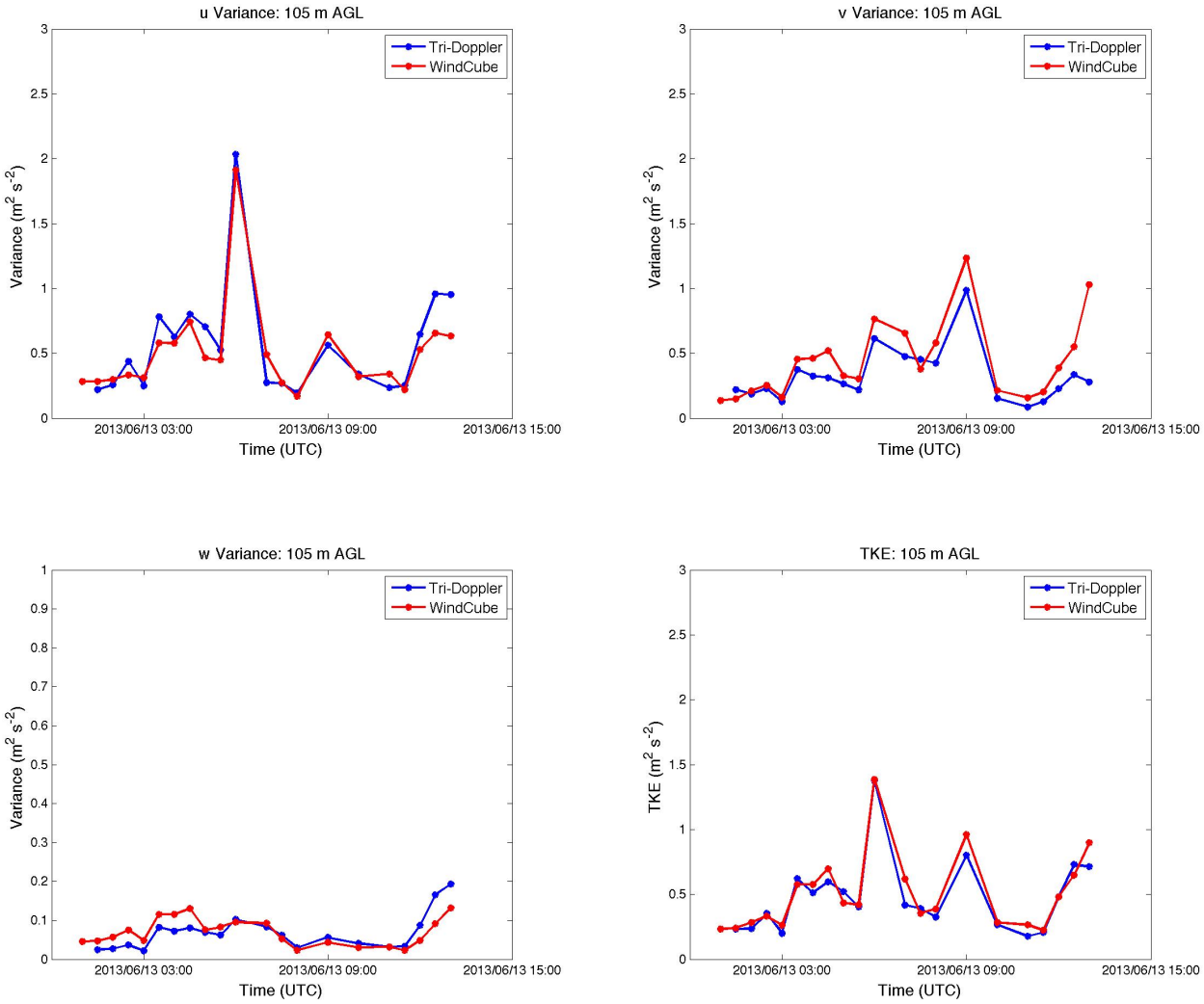

Figure 6: Rotated velocity variance and TKE from WindCube lidar and tri-Doppler technique at 105 m AGL on 13 June 2013.

present when the spectra were calculated with the radial velocity rather than the u and v velocities from the DBS technique. However, despite the variance contamination, the spectra agree quite well up until 0.25 Hz, when the WindCube spectra drop off rapidly due to the 4-s scan time. At the highest frequencies, the spectra for both lidars increase slightly, likely due to high-frequency noise in the velocity time series (e.g., Mann et al. 2008; Sjöholm et al. 2009). Spectra from both lidar techniques approximately follow the theoretical inertial subrange slope of -2/3 for intermediate frequencies but drop off due to volume averaging at the highest frequencies.

In comparison to the unstable spectra, the stable spectra peak at higher frequencies and have lower spectral energy (Fig. 9), as expected (Kaimal et al. 1972). There is no energy increase associated with velocity contamination, likely because the velocity contamination is not as prevalent under stable conditions (Sathe et al. 2011). Unlike the unstable spectra, the stable WindCube spectra appear to begin deviating from the tri-Doppler spectra slightly before the 0.25 Hz scanning frequency. Starting just after 0.1 Hz, the WindCube spectra begin dropping off and the tri-Doppler spectra start to have higher spectral energy than the WindCube spectra for all three velocity components. This suggests that the tri-Doppler technique can measure higher-frequency turbulence than the WindCube lidar under stable conditions, possibly due to the scanning circle used by the WindCube lidar. This difference is not evident

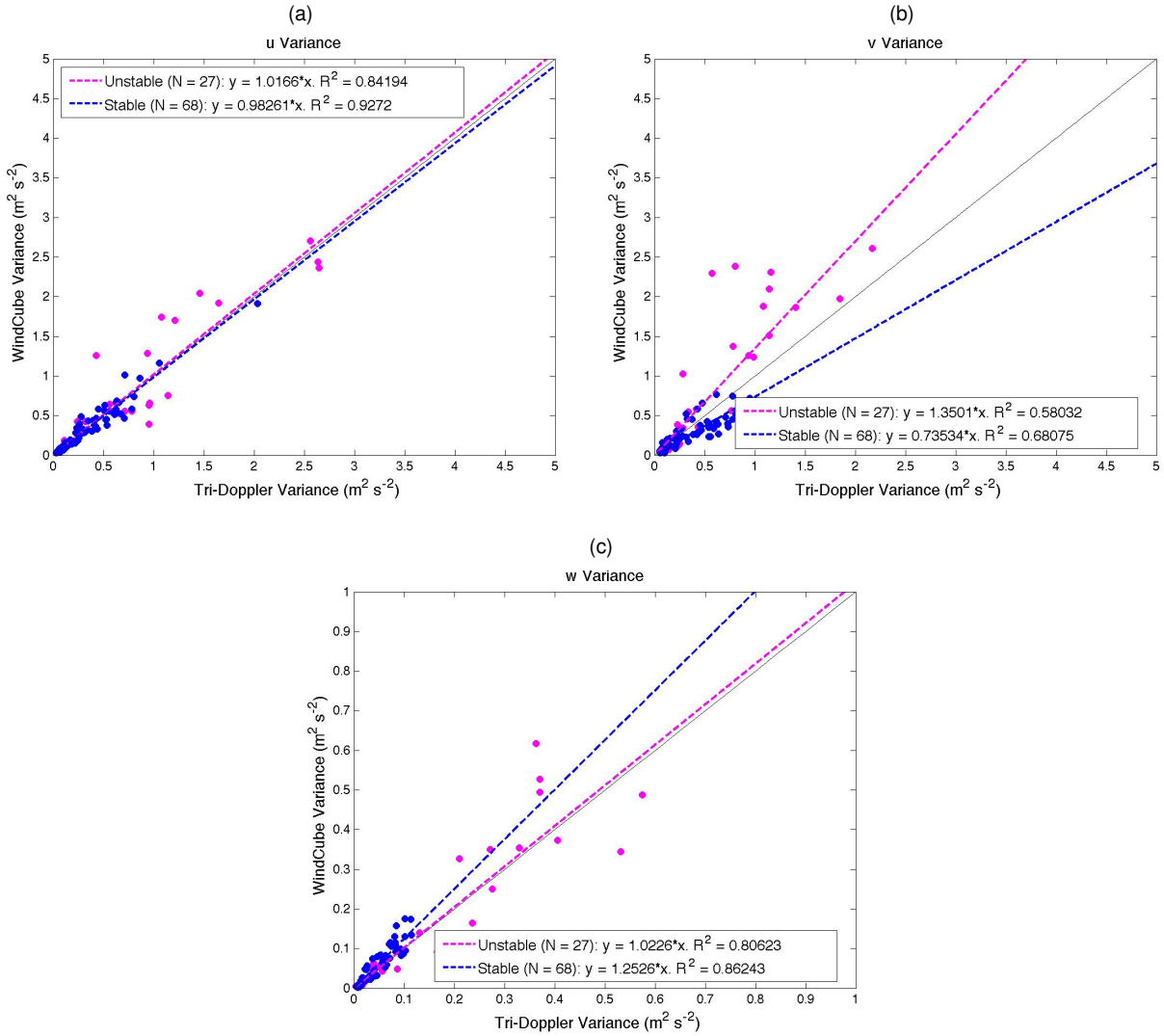

Figure 7: Scatter plots of tri-Doppler variance versus WindCube variance at 105 m AGL stratified by stability (circles) and regression lines for different stability classes (dashed lines). In all figures, one-to-one line is shown in black for reference. Scatter plots for a) u variance, b) v variance and c) w variance are shown. Data from neutral stability cases are not shown due to the small amount of data points in this stability classification.

under unstable conditions, as turbulence tends to occur on larger spatial and temporal scales (e.g., Stull 2000) and averaging within the WindCube scanning circle does not have a large effect on the measured velocity variance.

3.4. *Six-Beam Technique*

The six-beam technique proposed by Sathe (2012) was evaluated from 20 to 26 June 2013. The scanning strategy of the WindCube lidar cannot be modified to implement the six-beam technique, but the scanning lidars in the experiment were able to implement the technique. During this portion of the experiment, the Galion scanning lidar mimicked the scanning technique of the WindCube lidar, pointing the lidar beam toward the four cardinal directions then vertically upward in each DBS scan. In order to maximize the overlapping heights between the vertical range gates and the horizontal range gates, an elevation angle of 45° was used for the Galion scans. Unfortunately, this caused the Galion to have a larger scanning cone than the WindCube lidar, which uses an elevation

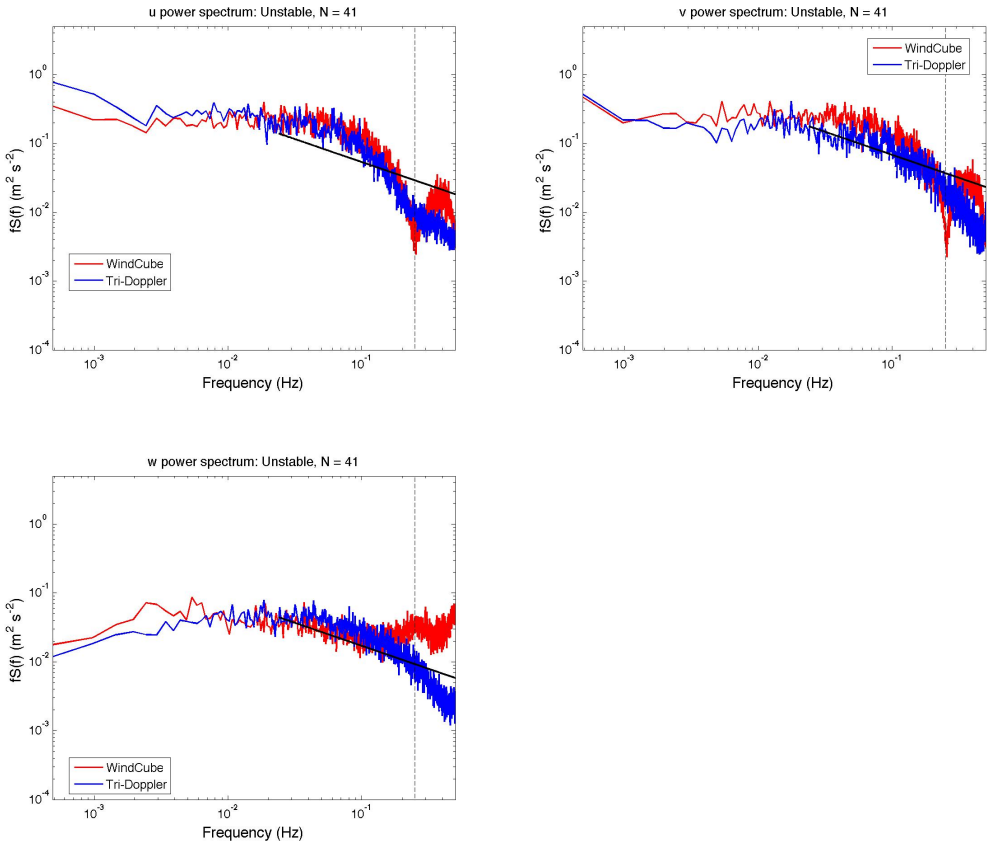

Figure 8: Average velocity spectra from tri-Doppler technique and WindCube lidar at 105 m AGL from 12 to 19 June 2013 under unstable conditions. Black solid line indicates -2/3 slope (inertial subrange). Black dotted line indicates 0.25 Hz WindCube frequency cut-off.

angle of 62°.

The OU Halo lidar employed the scanning strategy described by Sathe (2012), using an elevation angle of 45° and beams at 0, 72, 144, 216, and 288°, in addition to a vertical beam. The average variance of the radial velocity from each of the beams was used in Eq. 4 to produce six equations with six unknowns. The equations were then solved simultaneously to obtain values for the velocity variances and covariances from the OU Halo lidar.

Because the WindCube uses a simple rotating prism to steer the beam in different directions, it only takes one second for the WindCube to move from one beam position to another and accumulate measurements at the new beam position. In contrast, the scanning lidars need to mechanically move the scanner in elevation and azimuth and lock the scanner in place before taking measurements at each beam location. As a result, it takes approximately four seconds for the scanning lidars to move the beam to a different location and take measurements. For the six-beam technique, it took approximately 30 seconds for the OU Halo lidar to complete a single six-beam scan, so the radial velocity data from each beam were interpolated to a 30-s grid. In order to match the temporal resolution of the OU Halo lidar, the u, v, and w components of the WindCube and Galion lidars were also interpolated to a 30-s grid.

To calculate the variance from the DBS and six-beam scans, a similar technique to that employed with the tri-Doppler lidar data was used. The raw velocity data were first passed through a spike filter to remove outliers. The RFE (Eq. 8) and RN (Eq. 9) were calculated and used to flag data where the variance could be impacted by random errors or mesoscale variations. As before, the 30-min. averaged fluxes were used for the variance when no flag was present; otherwise, the fluxes were averaged over 60 min. While raw velocity data from the WindCube and Galion lidars were rotated into the 1-hour mean wind direction

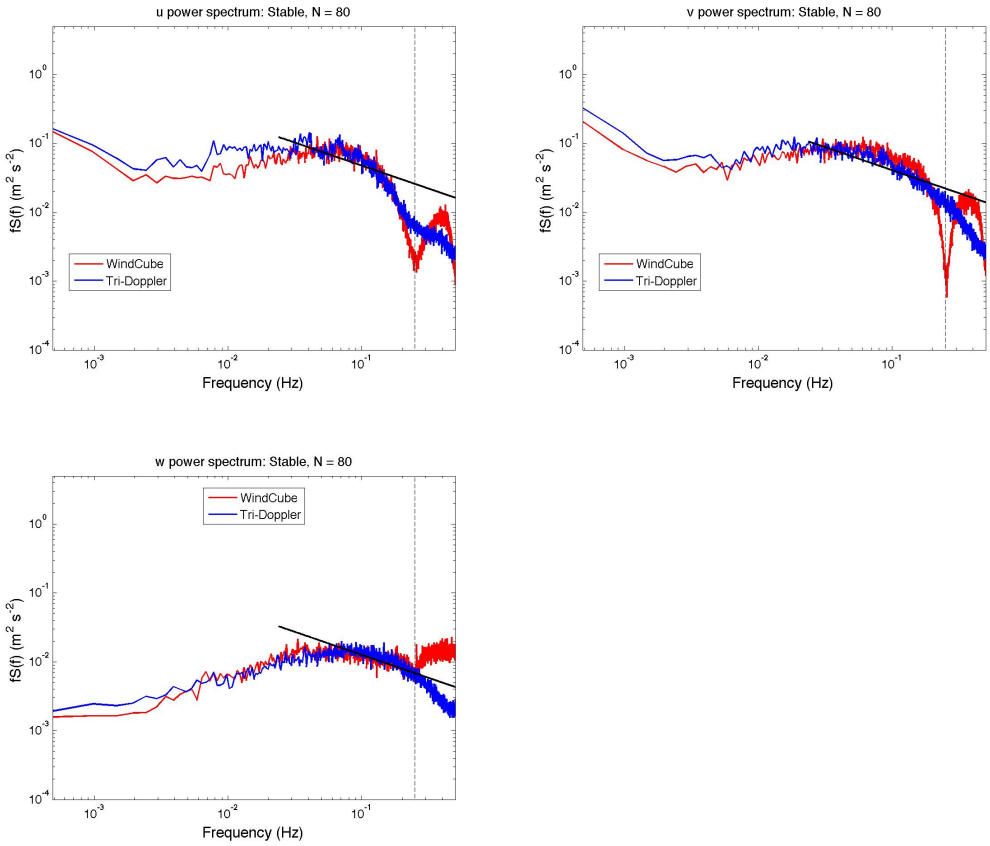

Figure 9: As in Fig. 8, but for stable conditions.

before the variance was calculated, the variance values from the six-beam technique needed to be rotated into the mean wind direction at the final step. The Velocity-Azimuth Display (VAD) technique (Browning and Wexler 1968) was used to calculate the mean wind direction from the OU Halo lidar to use for the coordinate rotation.

Sample velocity variance and TKE time series from the DBS and six-beam techniques are shown in Fig. 10. (Data from 74 m AGL are shown, which corresponds to the first useable range gate of the scanning lidars.) Although the WindCube and the Galion lidar were using very similar scanning strategies, the WindCube nearly always measured higher velocity variances. This likely occurred because the WindCube had both a smaller scanning circle and a smaller probe length in comparison to the Galion lidar. However, the variance measured by both lidars appears to follow similar temporal trends.

For the u and v variance, the Galion and OU Halo measured similar values, although the OU Halo measured slightly lower values toward the end of the time series, when convective conditions were beginning to dominate. This is expected, as the six-beam strategy used by the OU Halo lidar is designed to mitigate variance contamination, which is most prominent during unstable conditions. The vertical velocity variance measured by the OU Halo lidar was consistently higher than the variance measured by both the WindCube and the Galion lidars from the DBS technique. However, the vertical variance measured by all three lidars was similar when the data from the vertical beam only were used to calculate the vertical variance from the WindCube and Galion lidar data (Fig. 10). In short, higher vertical velocity variances were measured by the WindCube and Galion lidars when the radial velocity were collected in a probe volume directly above the lidar rather than from several points around a scanning circle. This allows the lidars to measure smaller scales of variance, which are averaged out in the scanning circle.

Scatter plots of the variance values measured at 74 m AGL throughout the six-beam portion of the experiment are shown in Fig. 11. For

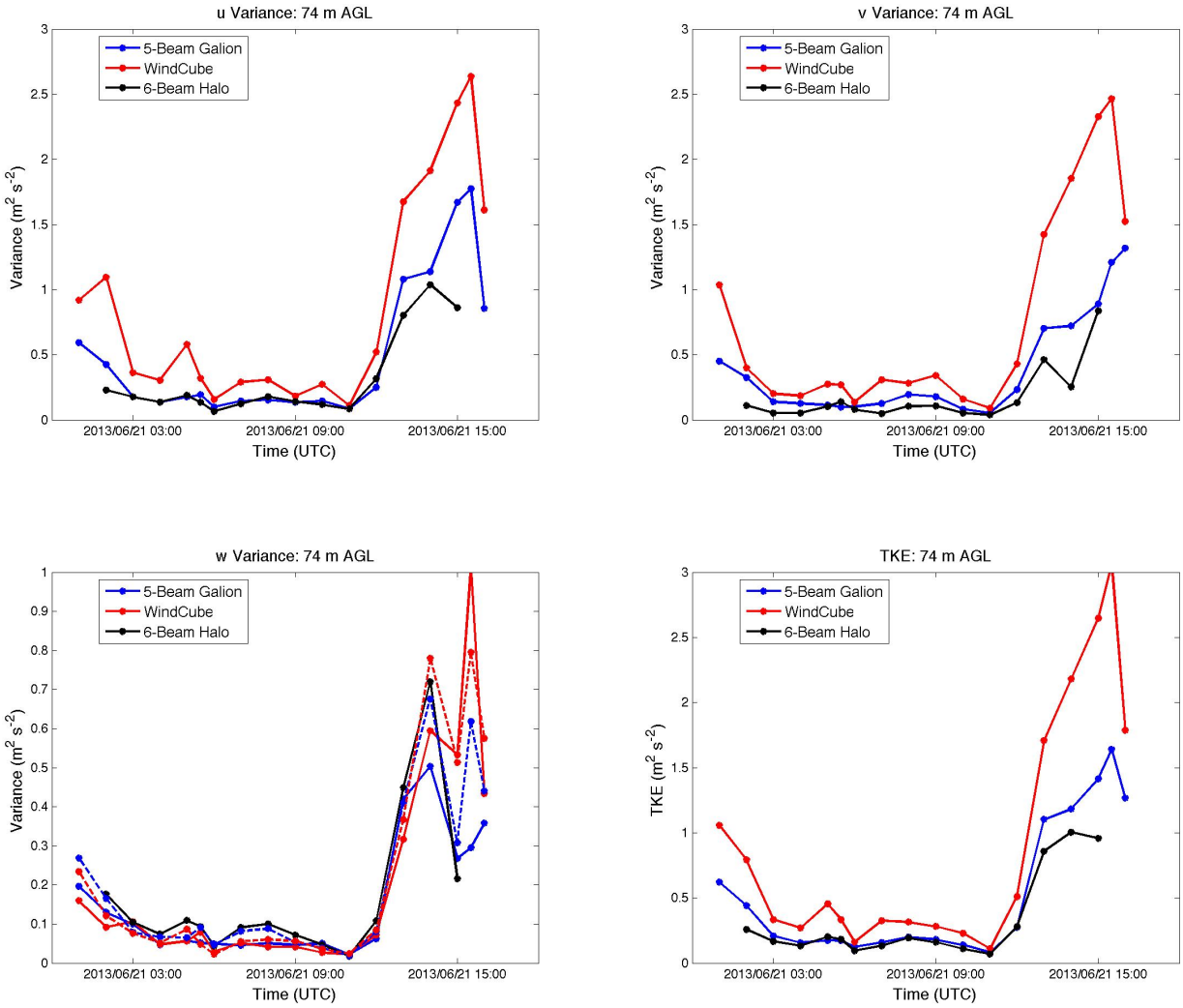

Figure 10: Rotated velocity variance and TKE from WindCube lidar, five-beam DBS technique used by the Galion lidar, and six-beam technique used by the OU Halo lidar at 74 m AGL on 21 June 2013. In w variance image, solid red and blue lines indicate vertical variance calculated from the DBS technique for the WindCube and Galion lidars, while dashed lines indicate variance calculated from the vertical beam of the lidars.

the u variance, the WindCube measured higher variance values than the Galion for both stable and unstable cases, nearly always measuring variances that were 75% larger than the Galion (Fig. 11a). This can likely be attributed to the smaller scanning circle and smaller range gate length used by the WindCube lidar. In contrast, the OU Halo lidar measured slightly smaller u variances than the Galion lidar for stable conditions, but measured significantly smaller variances for unstable conditions.

Variance trends were similar for the v component (Fig. 11b). Once again, the WindCube measured higher variance values than the Galion lidar for both stability classes. Trends for the OU Halo and Galion lidars were less pronounced. Similar to the u variance, the Galion tended to overestimate v variance values under unstable conditions. Under stable conditions, the Galion and OU Halo lidars measured similar values of the v variance at times, but the Galion tended to overestimate the v variance for other cases. It is possible that since the cross-wind variance is typically smaller than the along-wind variance (Panofsky 1962), the temporal resolution of the OU Halo lidar caused it to miss some of the smaller cross-wind turbulent eddies. While the Galion lidar updated the values of

(a)

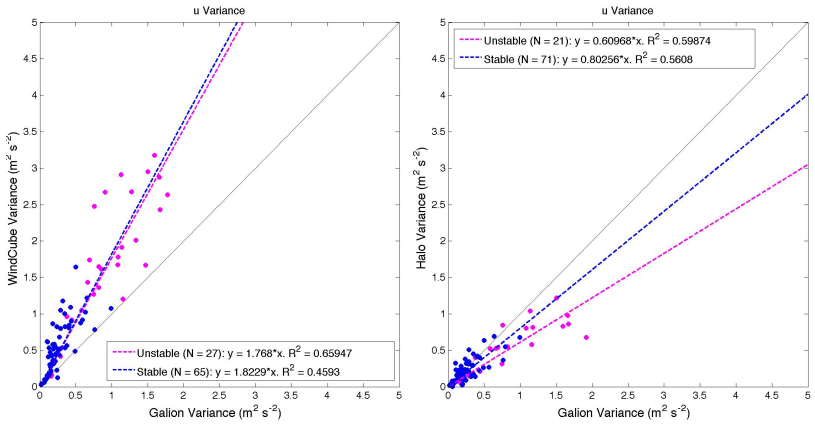

(b)

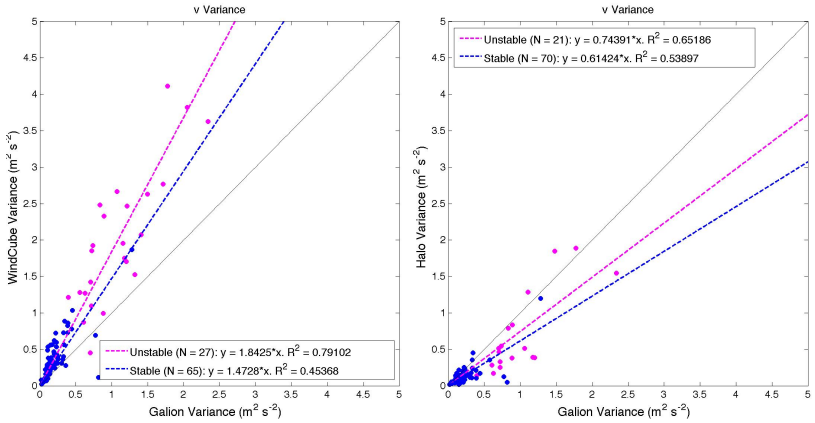

(c)

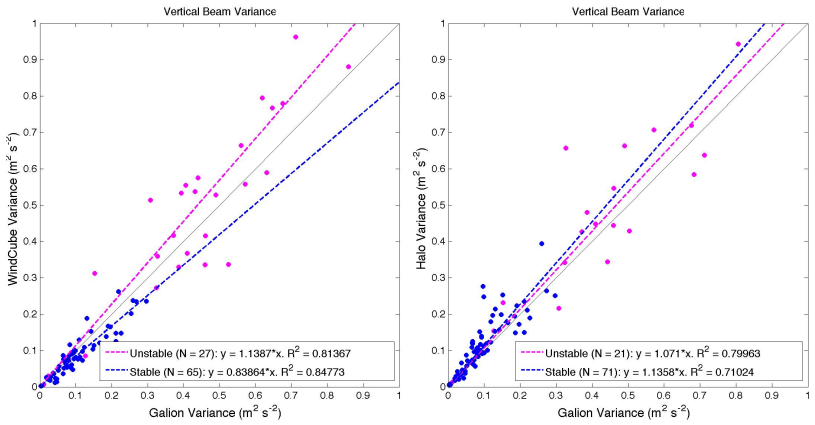

Figure 11: Scatter plot of a) u, b) v and c) w velocity variance from five-beam DBS technique used by the Galion lidar versus variance estimated by the WindCube lidar (left panels) and six-beam technique used by the OU Halo lidar (right panels) at 74 m AGL from 20 to 26 June 2013. Individual velocity variance values are denoted by circles and best-fit regression lines are shown with dashed lines. For all three lidars, only the velocity measurements from the vertically pointing beam were used to calculate the w variance. Data from neutral stability cases are not shown due to the small amount of data points in this stability classification.

u, v, and w every time the beam moved to a different position (i.e., every 4 s), the OU Halo lidar estimated the variance from velocity measurements that were taken 30 s apart in time. Although the velocity data from both lidars were interpolated to a 30-s grid, the Galion lidar may have still captured higher-frequency turbulence in the raw velocity data.

The Galion lidar measured slightly higher w variance than the WindCube lidar when just the vertical beam was used to calculate the variance, which eliminates averaging within the scanning circle (Fig. 11c). This is somewhat surprising, as the WindCube used a smaller range gate then the Galion lidar and was thus expected to measure higher w variance values. However, anecdotally, raw data from the scanning lidars tend to be more noisy than data from the WindCube lidar, so it is possible that some of the w variance measured by the Galion lidar was actually associated with random noise. The Galion and OU Halo lidars measured very similar vertical variance, which is expected since the lidar hardware is the same and the range gates used for both lidars were 30 m in length.

4. Summary and Conclusions

In this work, two different lidar scanning strategies, the tri-Doppler technique and the six-beam technique, were evaluated for their ability to measure low-level turbulence. A third scanning strategy, the virtual tower technique, will be evaluated in future work. These scanning strategies attempt to mitigate the systematic errors induced by typical DBS scans, including averaging over a scanning circle and contamination caused by cross-components of the Reynolds stress tensor.

The tri-Doppler technique involved pointing three scanning lidars at the same point in space and solving a set of equations to calculate u, v, and w every one second. Because the velocity data were not averaged over a scanning circle, this technique enabled the lidars to measure higher-frequency turbulence in comparison to a lidar using a DBS technique. This turbulence information was only available at the one height where the lidars were pointed. However, velocity data collected at other points along the two horizontal lidar beams can still be used to calculate the average wind speed profile (Klein et al. 2013). On an operational wind farm, this strategy could be designed to collect high-frequency turbulence measurements at the turbine hub height and collect average wind speed measurements at other heights across the rotor-disk area. Clearly, using three scanning lidars for a scanning strategy is mainly only feasible in a research setting. But a single scanning lidar could be pointed into the mean wind direction to measure line-of-sight turbulence and wind speed.

The six-beam technique only requires one lidar and could potentially be implemented into a small vertically pointing lidar with a rotating prism. By including six beams instead of the four or five that are typically used with a DBS scan, the six-beam technique can be used to decrease the variance contamination that is caused by cross-components of the Reynolds stress tensor. Although this was a limited data set, the six-beam technique did show a decrease in variance contamination under unstable conditions when compared to a similar lidar using a DBS scan. However, no sonic anemometer data were available at the heights scanned by the Halo lidars, so it is difficult to determine how accurately either of the scanning lidars were measuring variance. A recent field campaign that was conducted at a heavily instrumented site in Boulder, Colorado will provide a larger data set with sonic anemometer verification data. The same Halo lidar that was deployed at the ARM site was deployed at the Boulder site, so the Boulder campaign will provide insight into how accurately the Halo lidars can measure turbulence under a variety of stability conditions.

Although the ARM site experiment took place over a short period of time and did not feature a large amount of corresponding sonic anemometer and lidar data, it served as a feasibility experiment for the use of unique lidar scanning strategies. Several best practices, including techniques for lidar alignment and data processing, were learned during the experiment and later applied to the Boulder experiment. The tri-Doppler technique could be used with either three scanning lidars or a single scanning lidar (as a horizontal stare scan). This technique can provide high-frequency turbulence measurements at a single height and mean horizontal wind speeds at several heights. The six-beam technique showed promise for decreasing the effects of variance contamination under unstable conditions. This technique only requires one lidar and could potentially be implemented into a lidar with a rotating prism, such as a WindCube lidar.

5. ACKNOWLEDGMENTS

The authors would like to thank the staff of the Southern Great Plains ARM site, the members of the Boundary Layer Remote Sensing and Simulation group at OU, and the technical support staff at Sgurr Energy for their assistance during the experiment. In addition, we are grateful to Rob Newsom for sharing his lidar expertise and operating the ARM Halo lidar.

6. REFERENCES

Arya, S. P., 2001: *Introduction to Micrometeorology*, International Geophysics Series, Vol. 79. 2d ed., Academic Press, Cornwall, UK.

Bonner, W. D., 1968: Climatology of the low level jet. *Mon. Wea. Rev.*, **96**, 833–850.

Browning, K. A. and R. Wexler, 1968: The determination of kinematic properties of a wind field using Doppler radar. *J. Appl. Meteor.*, **7**, 105–113.

Cañadillas, B., A. Westerhellweg, and T. Neumann, 2011: Testing the performance of ground-based wind LiDAR system. *DEWI Magazine*, **(38)**, 58–64.

Calhoun, R., R. Heap, M. Princevac, R. Newsom, H. Fernando, and D. Ligon, 2006: Virtual towers using coherent Doppler lidar during the Joint Urban 2003 Dispersion Experiment. *J. Appl. Meteor.*, **45**, 1116–1126.

Cariou, J.-P. and M. Boquet, 2010: LEOSPHERE Pulsed Lidar Principles. Contribution to UpWind WP6 on Remote Sensing Devices. [Available online at `http://www.upwind.eu/Publications/~/media/UpWind/Documents/Publications/6%20-%20Remote%20Sensing/D611.ashx`.].

Eberhard, W. L., R. E. Cupp, and K. R. Healy, 1989: Doppler lidar measurement of profiles of turbulence and momentum flux. *J. Atmos. Oceanic Technol.*, **6**, 809–819.

Elliott, D. L. and J. B. Cadogan, 1990: Effects of wind shear and turbulence on wind turbine power curves, *Proc. European Community Wind Energy Conference and Exhibition.*, Madrid, Spain.

Højstrup, J., 1993: A statistical data screening procedure. *Measurement Science and Technology*, **4**, 153–157.

Huffaker, R. M. and R. M. Hardesty, 1996: Remote sensing of atmospheric wind velocities using solid-state and CO_2 coherent laser systems. *Proceedings of the IEEE*, **84**, 181–204.

Kaimal, J. C., J. C. Wyngaard, Y. Izumi, and O. R. Coté, 1972: Spectral characteristics of surface-layer turbulence. *Quart. J. Roy. Meteor. Soc.*, **98**, 563–589.

Kelley, N. D., B. J. Jonkman, and G. N. Scott, 2006: The Great Plains turbulence environment: Its origins, impact and simulation. NREL/CP-500-40176. National Renewable Energy Laboratory, 21 pp.

Klein, P., J. Newman, T. Bonin, and S. Wharton, 2013: Lidar measurements of wind and turbulence for wind-energy applications, *North American Wind Energy Academy Symposium*, Boulder, CO.

Lundquist, J., L. Glascoe, and J. Obrech, 2010: Operational forecasting based on a modified Weather Research and Forecasting model, Preprints, *5th International Symposium on Computational Wind Engineering*, Chapel Hill, NC. International Association for Wind Engineering.

Mahrt, L., D. Vickers, J. Howell, J. Højstrup, J. M. Wilczak, J. Edson, and J. Hare, 1996: Sea surface drag coefficients in the Risø Air Sea Experiment. *J. Geophys. Res.: Oceans*, **101**, 14 327–14 335.

Mann, J., et al., 2008: Comparison of 3D turbulence measurements using three staring wind lidars and a sonic anemometer. *IOP Conference Series: Earth and Environmental Science*, **1**, 012 012.

Panofsky, H. A., 1962: Scale analysis of atmospheric turbulence at 2 m. *Quart. J. Roy. Meteor. Soc.*, **88**, 57–69.

Panofsky, H. A. and J. A. Dutton, 1984: *Atmospheric Turbulence: Models and Methods for Engineering Applications*. John Wiley & Sons, Inc., 397 pp.

Pearson, G., F. Davies, and C. Collier, 2009: An analysis of the performance of the UFAM pulsed Doppler lidar for observing the boundary layer. *J. Atmos. Oceanic Technol.*, **26**, 240–250.

Sathe, A., 2012: Influence of wind conditions on wind turbine loads and measurement of turbulence using lidars. Ph.D. thesis, Delft University Wind Energy Research Institute, Lyngby, Denmark.

Sathe, A. and J. Mann, 2012a: Measurement of turbulence spectra using scanning pulsed wind lidars. *J. Geophys. Res.: Atmospheres*, **117**.

Sathe, A. and J. Mann, 2012b: Turbulence measurements using six lidar beams. *Extended Abstracts of Presentations from the 16th International Symposium for the Advancement of Boundary-Layer Remote Sensing*, Steering Committee of the 16th International Symposium for the Advancement of Boundary-Layer Remote Sensing, 302–305.

Sathe, A., J. Mann, J. Gottschall, and M. S. Courtney, 2011: Can wind lidars measure turbulence? *J. Atmos. Oceanic Technol.*, **28**, 853–868.

Sjöholm, M., T. Mikkelsen, J. Mann, K. Enevoldsen, and M. Courtney, 2009: Spatial averaging-effects on turbulence measured by a continuous-wave coherent lidar. *Met. Zeit.*, **18**, 281–287.

Song, J., K. Liao, R. L. Coulter, and B. M. Lesht, 2005: Climatology of the low-level jet at the Southern Great Plains Atmospheric Boundary Layer Experiments site. *J. Appl. Meteor.*, **44**, 1593–1606.

Strauch, R. G., D. A. Merritt, K. P. Moran, K. B. Earnshaw, and D. V. De Kamp, 1984: The Colorado Wind-Profiling Network. *J. Atmos. Oceanic Technol.*, **1**, 37–49.

Stull, R. B., 2000: *Meteorology for Scientists and Engineers*. 2d ed., Brooks Cole, 528 pp.

Sumner, J. and C. Masson, 2006: Influence of atmospheric stability on wind turbine power performance curves. *Journal of Solar Energy Engineering*, **128**, 531–538.

Taylor, G. I., 1938: The spectrum of turbulence. *Proceedings of the Royal Society of London. Series A - Mathematical and Physical Sciences*, **164**, 476–490.

Vickers, D. and L. Mahrt, 1997: Quality control and flux sampling problems for tower and aircraft data. *J. Atmos. Oceanic Technol.*, **14**, 512–526.

Wagner, R., I. Antoniou, S. M. Pedersen, M. S. Courtney, and H. E. Jørgensen, 2009: The influence of the wind speed profile on wind turbine performance measurements. *Wind Energy*, **12**, 348–362.

Wharton, S. and J. K. Lundquist, 2012: Atmospheric stability affects wind turbine power collection. *Environ. Res. Lett.*, **7**, 014 005.

Wilczak, J. M., S. P. Oncley, and S. A. Stage, 2001: Sonic anemometer tilt correction algorithms. *Bound.-Layer Meteor.*, **99**, 127–150.